Supercontinuum noise reduction by fiber undertapering

Engelsholm, Rasmus Dybbro; Bang, Ole

Published in:
Optics Express

Link to article, DOI:
10.1364/OE.27.010320

Publication date:
2019

Document Version
Publisher's PDF, also known as Version of record

Research Article | Vol. 27, No. 7 | 1 Apr 2019 | OPTICS EXPRESS 10320
Optics EXPRESS

Supercontinuum noise reduction by fiber undertapering

RASMUS DYBBRO ENGELSHOLM[1,3] AND AND OLE BANG[1,2,4]

[1]DTU Fotonik, Department of Photonics Engineering, Building 343, Ørsteds Plads, Technical University of Denmark, 2800 Kgs. Lyngby, Denmark
[2]NKT Photonics A/S, Blokken 84, 3460 Birkerød, Denmark
[3]raseng@fotonik.dtu.dk
[4]oban@fotonik.dtu.dk

Abstract: We demonstrate that the Relative Intensity Noise (RIN) of a supercontinuum source can be significantly reduced using the new concept of undertapering, where the fiber is tapered to a diameter that is smaller than the diameter that gives the shortest blue edge, which is typically regarded as the optimum. We show that undertapering allows to control the second zero dispersion wavelength and use it as a soliton barrier to stop the red shifting solitons at a pre-defined wavelength, and thereby strongly reduce the RIN. We demonstrate how undertapering can reduce the spectrally averaged RIN in the optical coherence tomography bands, 500 – 800 nm and 1150 – 1450 nm, by more than a factor two.

1. Introduction

Supercontinuum generation (SCG) has been an active research topic for the past 30 years, and most of the processes behind the broad spectrum are currently well understood, [1,2]. Supercontinuum sources have found applications in many fields due to their exceptional spectral bandwidth and brightness, despite their often poor noise properties compared to alternative choices. Recently, a lot of work has been carried out within the field of SC-based Spectral Domain Optical Coherence Tomography (SD-OCT), [3–8], with a focus on the visible and near infrared wavelength ranges of 500 – 800 nm and 1150 – 1450 nm. A common trend in the conclusions of this work is that there is a need for SC sources with lower noise, as the noise directly influences the background noise and thus both contrast and image quality.

The noise properties of the SC, and especially how to control and reduce it for the different types of SCG methods, is still an active research field as seen by recent work, [9–16]. The methods of SCG range from femtosecond pulse broading due to self-phase modulation in normal dispersion fibers, to soliton fission or modulational instability (MI) induced pulse breakup for anomalous dispersion fibers. In this paper we will focus entirely on reducing the noise for MI-base SC sources, since they are the most noisy and since all high-power commercial sources are based on this technology today [10]. Modulation instability breaks up the pulse in a large number of fundamental solitons, which then redshift, collide and combine with each other in a chaotic manner [1, 17]. This results in large pulse-to-pulse fluctuations of the distribution of solitons, which makes it a rare event that several smaller solitons combine into one big soliton, or rogue wave, that can Raman red-shift all the way to the loss edge. This means that the Relative Intensity Noise (RIN) is increasing towards the edge, where it has been observed that the pulse energy statistics becomes L-shaped and resembles that of rogue waves [9, 18]. The power and hence the noise at the blue edge is linked to that of the red edge through trapped Dispersive Waves (DWs) [19, 20], which was thoroughly investigated in tapers [21–26].

The noise of a high power SC is largely unaffected by attempts to control the breakup process by for instance seeding [27], although some headway has been made at low powers where the soliton dynamics is less chaotic [27–29]. For example, pumping a PCF with pitch 3.6μm and

#352783 https://doi.org/10.1364/OE.27.010320
Journal © 2019 Received 27 Nov 2018; revised 4 Jan 2019; accepted 6 Jan 2019; published 29 Mar 2019

Optics EXPRESS

relative hole diameter 0.52 at 1064nm close to the zero-dispersion wavelength (ZDW) with 3ps pulses, allows to stabilize the SC with seeding for less than 500W pump peak power, but not for larger than 1.5kW pump peak power [27]. Weak tapering has previously been investigated as a means to improve the noise, without notable improvements, [10]. Tapering in general has also been used to control the spectral bandwidth of the generated light, [1, 21, 30, 31], but without considering noise. The effect of pumping in the anomalous dispersion regime in between two closely spaced ZDWs or close to the second ZDW has also been investigated, [32–34]. The focus of this paper will be in the overlap of these avenues of research, to investigate tapering in which the presence of a second ZDW is used as a barrier [35, 36] to control the redshifting solitons responsible for the adverse RIN properties at the spectral edges.

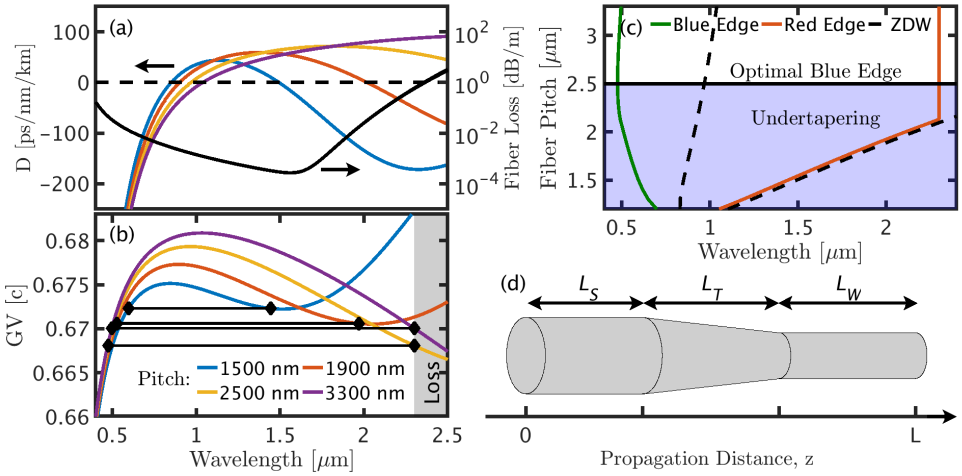

Fig. 1. (a+b) Fiber dispersion (D), total loss and Group Velocity (GV) normalized to the speed of light for PCFs with 10 rings of holes in a hexagonal structure with a fixed hole diameter to pitch ratio of 0.52 and varying pitch. The 4 loss curves are all black. (c) Predicted spectral SC edges versus pitch found by GV matching the blue edge to the red edge (marked with diamonds and black lines in (b)), with the red edge being defined as the minimum of either the second ZDW or the loss edge (2300 nm) [21]. The colored area marks the area of undertapering. (d) Illustration of the length scales L_S, L_T, and L_W of the investigated tapers.

As a generic example, we consider a specific Photonic Crystal Fiber (PCF) with hole diameter to pitch ratio of d/Λ=0.52 [22,27], which is widely used because it is single-mode at 1064 nm [37]. This PCF has the dispersion, group velocity and spectral edges as seen in Figs. 1(a)-1(c), where we note that the total loss is the same for the 4 PCFs and thus dominated by material loss. The investigated taper profile is shown in Fig. 1(d), and consists of a straight section of length L_S, followed by a piece of linear down-tapering of length L_T, ending in a straight piece of taper waist of length L_W. We consider as pump laser a standard high average power picosecond (ps) ytterbium fiber laser with the specifications given in Table 1. We will focus our investigation on the spectrally averaged RIN in two of the most important spectral ranges of interest to the field of SD-OCT. The spectrally averaged RIN provides a single measure of the noise in the band of interest and is calculated as

$$\langle RIN(\lambda)\rangle_{\lambda_1}^{\lambda_2} \equiv \frac{\int_{\lambda_1}^{\lambda_2} PSD(\lambda)\, RIN(\lambda)\, \mathrm{d}\lambda}{\int_{\lambda_1}^{\lambda_2} PSD(\lambda)\, \mathrm{d}\lambda}. \quad (1)$$

Optics EXPRESS

Table 1. Specifications of the pump laser used in all simulations. The pump pulse is assumed to be Gaussian shaped with no chirp. The specifications are for the pulse power envelope, $P(t)$.

T_{FWHM}	Peak Power	Rep. Rate	Wavelength	Shape	Av. Power
7 ps	7 kW	80 MHz	1064 nm	$\sqrt{P_0}\exp[-t^2/(2T_0^2)]$	4.17 W

The Power Spectral Density (PSD) follows the usual definition, while the RIN is defined as,

$$RIN(\lambda) = \sqrt{\frac{\langle E_n^2(\lambda)\rangle - \langle E_n(\lambda)\rangle^2}{\langle E_n(\lambda)\rangle^2}} \tag{2}$$

where $E_n(\lambda)$ is the energy of a single pulse in the wavelength interval from $\lambda - \Delta\lambda/2$ to $\lambda + \Delta\lambda/2$. Throughout this paper $\Delta\lambda = 10$ nm, corresponding to commercially available standard filters used in several earlier noise investigations, [10, 12, 25].

2. Simulation methods

All simulations presented in this paper were done in two steps. In the first step the fiber properties, such as the complex propagation constant, β, and the power normalized transverse mode profile, $\widehat{\mathcal{E}}$, were calculated by the Finite Element Method in COMSOL for the various frequencies (every 2 THz) and taper steps (every $\Lambda = 100$ nm).

In the second step these were interpolated and used in a single mode, single polarization, implementation of the envelope Generalized Non-Linear Schrödinger Equation (GNLSE). The equation was derived neglecting third harmonic generation and the double rotating Raman term, assuming slow tapering, and assuming the transverse field overlap integral to be independent of the different conjugation permutations. This follows closely the work of others [38–42] and means that the fractional Raman contribution is $f_r = 0.18$. The full equation solved under these approximations is

$$\begin{aligned}\frac{\partial}{\partial z}\left[\left[\exp(i\phi(\Omega,z))\right]^*\tilde{C}(\Omega,z)\right] &= i\gamma(\Omega,z)\left[\exp(i\phi(\Omega,z))\right]^*\\ \mathcal{F}\Big[\mathcal{F}^{-1}\left[\tilde{C}(\Omega,z)K(\Omega,z)\right]\mathcal{F}^{-1}\Big[\tilde{R}(\Omega)\\ \mathcal{F}\left[\mathcal{F}^{-1}\left[\tilde{C}(\Omega,z)K(\Omega,z)\right]^*\mathcal{F}^{-1}\left[\tilde{C}(\Omega,z)K(\Omega,z)\right]\right]\Big]\Big] &,\end{aligned} \tag{3}$$

where

$$\begin{aligned}\gamma(\Omega,z) =& \frac{3}{16}\epsilon_0\Omega\tilde{\chi}^{(3)}_{xxxx}K(\Omega,z)\\ &\int\int\widehat{\mathcal{E}}^*(\Omega_0,x,y,z)\cdot\widehat{\mathcal{E}}(\Omega_0,x,y,z)\,\widehat{\mathcal{E}}^*(\Omega_0,x,y,z)\cdot\widehat{\mathcal{E}}(\Omega_0,x,y,z)\,\mathrm{d}x\mathrm{d}y,\end{aligned} \tag{4}$$

$$K(\Omega,z) = \left[\frac{\int\int\left[\widehat{\mathcal{E}}^*(\Omega,x,y,z)\cdot\widehat{\mathcal{E}}(\Omega,x,y,z)\,\widehat{\mathcal{E}}^*(\Omega,x,y,z)\cdot\widehat{\mathcal{E}}(\Omega,x,y,z)\right]\mathrm{d}x\mathrm{d}y}{\int\int\left[\widehat{\mathcal{E}}^*(\Omega_0,x,y,z)\cdot\widehat{\mathcal{E}}(\Omega_0,x,y,z)\,\widehat{\mathcal{E}}^*(\Omega_0,x,y,z)\cdot\widehat{\mathcal{E}}(\Omega_0,x,y,z)\right]\mathrm{d}x\mathrm{d}y}\right]^{\frac{1}{4}}, \tag{5}$$

and mode profile dispersion is included through the parameter $K(\Omega,z)$ such as to conserve the photon number. Ω is the physical frequency, $\phi(\Omega,z) = \int_0^z\sum_{n=2}^{\infty}\frac{\beta_n(z')}{n!}(\Omega-\Omega_0)^n\,\mathrm{d}z'$ is the

Optics EXPRESS

accumulated phase minus the first order term at the pump frequency, Ω_0, and $\beta_n(z')$ are the expansion terms of the propagation constant at Ω_0. The propagation constant is complex and includes both confinement loss and silica material loss [43]. Tilde and non-tilde variables denote a Fourier domain and time domain pair, $\mathcal{F}[]$ is the Fourier transform, $\tilde{C}(\Omega, z) = \tilde{\mathcal{A}}(\Omega, z)\exp(i\phi(\Omega, z))$ where $\mathcal{A}(t, z)$ is the envelope in time with units $\sqrt{\mathrm{W}}$, $\widehat{\mathcal{E}}(\Omega_0, x, y, z)$ is the power normalized transverse electric field, ϵ_0 is the vacuum permittivity and $\tilde{R}(\Omega) = \left[(1 - f_r) + f_r \tilde{h}_r(\Omega)\right]$ is the nonlinear response function where $\tilde{h}_r(\Omega)$ is the full measured Raman gain profile of silica [2, 44], and $\tilde{\chi}^{(3)}_{xxxx} = 1.32 \cdot 10^{-22}\,\mathrm{m^2V^{-2}}$ is calculated from the $n_2 = 2.36 \cdot 10^{-20}\,\mathrm{m^2W^{-1}}$ value listed in table 11.1 in Agrawal [2].

The equation was solved using the Runge-Kutta-Fehlberg method to obtain both 4th and 5th order solutions. The comparison of these two solutions was then used to automatically adapt the step size, in order to keep the relative error within a predefined tolerance. The local error was defined as the L^2-norm of the difference between the 4th and 5th order solutions normalized to the number of discretization points. All simulations started at and were limited to a step length of maximally 100 μm, usually adapting down to about 5 μm when the nonlinear interaction was strongest, before slowly increasing again. The upper limit was necessary to keep the step length short in order to prevent error accumulation in the initial stages of MI, where the modulation is barely above the noise floor. We have in all our simulations included quantum noise, modelled semi-classically as the standard one-photon per mode noise, which is added to the initial condition in the Fourier domain [1, 45]. We measured the RIN of our pump laser in the lab. to be 1% and therefore also added an input peak power noise of 1% to make the modelling more realistic. Recent studies showed that adding the RIN of the pump gave better correspondence between the modelled SC noise and the experimentally found SC noise [16, 46].

All simulations were done using first COMSOL 5.1 on a generic computer and then MATLAB utilizing a GV100 Volta (2017) Nvidia GPU. The transverse integration was performed over only the regions containing glass, so any nonlinear interaction arising inside the air holes is neglected.

Evaluating $\gamma(\Omega, z)$ at Ω_0, we recover the classical nonlinear coefficient $\gamma(\Omega_0, z)$ which is $8.3\,\mathrm{W^{-1}km^{-1}}$ at 1040 nm and $5.2\,\mathrm{W^{-1}km^{-1}}$ at 1550 nm in the initial straight fiber and $33\,\mathrm{W^{-1}km^{-1}}$ at 1040 nm and $16.6\,\mathrm{W^{-1}km^{-1}}$ at 1550 nm in the taper waist for $\Lambda = 1.5$ μm. This shows how the enhancement of the nonlinearity by tapering is significant and wavelength dependent.

The numerical implementation was checked by simulating several known analytical cases, such as theoretical MI sideband position, single soliton propagation and more. For all simulations a time and frequency discretization of $N = 2^{19}$ points were used with an equidistant time spacing of $\Delta t = 0.92$ fs. Each ensemble had an ensemble size of $N_E = 50$. A choice of 20-128 is a standard number. In the early classical SC noise papers [1, 47] 20 simulations was used and in [48, 49] 128 was used. In the high power ps cases we consider here 100 simulations was used and shown to be sufficient in [26]. We here repeated a few selected cases with an ensemble of 100 pulses and found no noticeable difference. All presented spectral data was rebinned to 10 nm intervals. For the RIN analysis, this corresponds to measuring the pulse-to-pulse noise of light with perfect 10 nm bandpass filters.

3. Results and discussion

In Figs. 2(a) and 2(b) the evolution of the PSD in 10 m untapered fiber ($\Lambda = 3.3$ μm) and 2 m of a fiber tapered to obtain an optimal blue edge ($\Lambda = 2.5$ μm) is shown. In Figs. 2(e) and 2(f) we see the corresponding evolution of the RIN. Both these cases have been studied in depth before, both numerically and experimentally [10, 21, 50], which makes them ideal to use as a baseline. While the spectrum continues to broaden with propagation, we can see that the noise does not change much as soon as we are sufficently far away from the spectral edges. This is in agreement with previous work [10, 21, 50] and as we shall see, the reason is that the second ZDW is not coming into play.

Optics EXPRESS

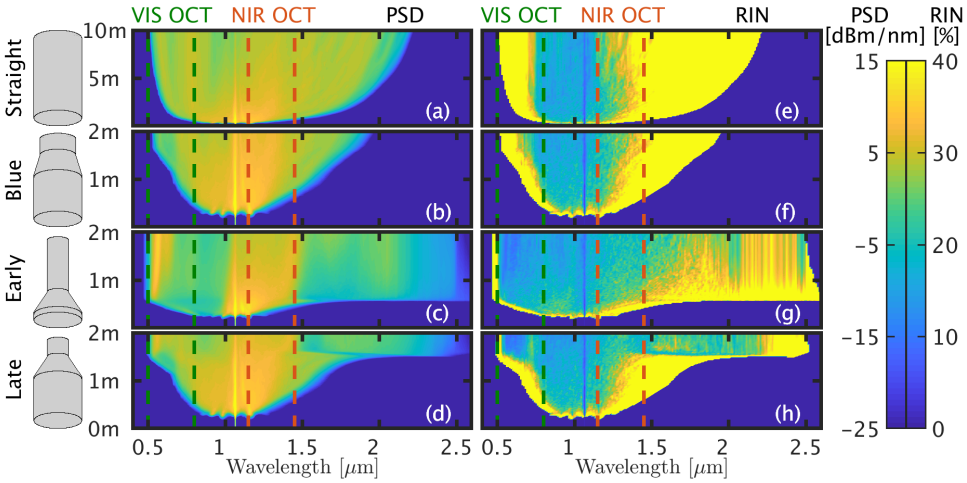

Fig. 2. Simulated ensemble averaged PSD and RIN evolution in various fibers shown on the left side. *Straight*: Untapered 3.3 μm pitch for $L_s = 10$ m *Blue*: Fiber tapered from 3.3 μm to 2.5 μm pitch, with $L_s = 1.1$ m, $L_T = 0.5$ m and $L_W = 0.4$ m. *Early*: Fiber tapered from 3.3 μm to 1.5 μm pitch, with $L_s = 0.1$ m, $L_T = 0.5$ m and $L_W = 1.4$ m *Late*: Fiber tapered from 3.3 μm to 1.5 μm pitch, with $L_s = 1.1$ m, $L_T = 0.5$ m and $L_W = 0.4$ m. Note that for all cases the RIN is only shown when the PSD is higher than −20 dBm/nm. The scaling has been chosen to best show the noise in the NIR OCT band. Near the spectral edge the RIN can reach values in excess of 100 %

In the last two rows of Fig. 2, we investigate two cases of undertapering the fiber down to a pitch of $\Lambda = 1.5$ μm, to reduce the RIN by clamping the solitons at the second ZDW. In the figure the two OCT bands of interest are marked. In the *Early* design, Figs. 2(c) and 2(g), the fiber is tapered early on so that the second ZDW reaches its final wavelength at 1500 nm before any significant power has reached this wavelength. In the *Late* case, Figs. 2(d) and 2(h), the tapering is initiated 1 m later to investigate the noise in the case where the second ZDW spectrally moves through the redshifting solitons.

In both the *Early* and *Late* cases we see a large build-up at the blue edge, starting at 535 nm in the taper transition and then shifting to around 565 nm in the taper waist. A 10 kW peak power soliton at 1080 nm has phasematching to 565 nm but cannot directly generate a dispersive wave at this position, as there is no spectral overlap. The solitons from the sea of solitons generated around the MI stokes wavelength can however trap light close to the pump wavelength and spectrally push it into this region when they themselves redshift to the second ZDW. The nonlinearity is enchanced in the taper, which enhances MI from the remainder of the pump and speeds up the process. The redshift rate is also strongly increased by the decreasing dispersion close to the second ZDW. The rate of depletion of the pump after 1 m of propagation was found to closely match the increase in power around 565 nm.

In the *Early* design, after the initial broadening beyond 2 μm at the start of the fiber waist, the power transfer to the red side of the second zero dispersion wavelength slows down. While the power is steady, the noise in this region is gradually improved. The spectrum is clearly still noisy at the edges, but at the same time there are clear improvements compared to the *Blue* and *Straight* designs. In the *Late* case we see the same spectral buildup as in the *Early* case, but the noise properties look excellent right away, without the need for the light to propagate some distance in the taper waist to settle. There is a clear drop in power visible around the second ZDW as it moves in from the red edge. Established theory would tell us that solitons are recoiled

Optics EXPRESS

and prevented from existing right at the second ZDW [33, 36]. In both cases we can observe how the losses in the taper start to eat away at the red edge. This is especially clear from the −20 dBm/nm edge cutoff on the RIN plots.

For a more detailed view, the output PSD and RIN spectra of the four cases can be seen in Fig. 3. The straight fiber and the *Blue* design have similar noise properties, with the long wavelength noise almost coinciding, while at the blue edge the noise edge is moved slightly (75 nm) out for the taper. From earlier work [10, 21, 50], we would expect an extended blue edge compared to the straight fiber, which is not the case in the figure. This is simply because the *Blue* design has not yet reached its full spectral extension after 2 m of propagation.

For all four cases there is a gap on the blue side of the pump. It is least pronounced for the *Blue* design, and most for the *Early* and *Late* designs. For all cases it is centered around the first ZDW in the taper waist, which shifts to shorter wavelengths the more the fiber is tapered. The first ZDW is 1040 nm for the *Straight* design, 970 nm for the *Blue* design and 860 nm for both the *Early* and *Late* designs. The 10 m *Straight* fiber has the most depleted pump with only 3.6 dBm/nm remaining, mainly due to its length. Of the remaining 2 m long fibers, the *Blue* design has the least depleted pump with 9.9 dBm/nm remaining, while the *Late* has 7.9 dBm/nm remaining and the *Early* has 5.6 dBm/nm remaining. The increased pump depletion matches well with the increased power in the blue edge. As expected, we see there is a huge dip in the power spectral density for the *Early* and *Late* fibers, at the second ZDW at 1500 nm. The dip is larger for the *Late* design (8.1 dBm/nm) than for the *Early* design (5.1 dBm/nm). In terms of noise, we now clearly see that both the *Early* and *Late* tapers have approximately the same noise in the whole region of interest, which is significantly lower than the *Straight* and *Blue* designs outside the pump region 700-1200 nm. This noise reduction property of undertapering has been patented [51], but never properly explained and published in the scientific literature. Below we explain in detail the effects behind this property.

In Figs. 4(a) and 4(b) the integrated power and weigthed RIN in the bands of interest is shown as a function of propagation distance for the four cases described in Figs. 2 and 3. Since the *Straight*, *Blue* and *Late* cases have the exact same parameters in the first 1.1 m of fiber, these curves should be identical in this region. The slight differences observed in the weighted RIN is because we have used different noise seeds in the three cases. Looking at the noise, we observe

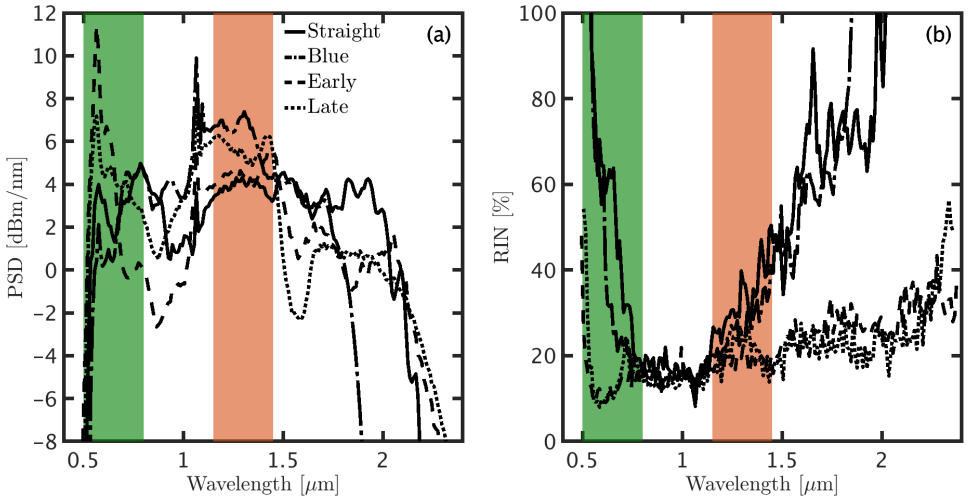

Fig. 3. PSD and RIN at the output the four cases shown in Fig. 2. The green and red areas mark the spectral ranges that are of interest for visible and near infrared OCT.

the clear trend that undertapering improves the noise significantly and that in general longer propagation is better, but that the improvement eventually saturates. For the VIS band, which is at the spectral edge of the SC, the power continuously increases as more and more DWs reach the edge. In contrast the NIR band is in the interior of the SC spectrum and therefore has a strong increase initially when the solitons reach the region, after which it gradually decreases as the solitons pass through. Thus noise improvement always has to be balanced against the required power.

We continue the investigation by looking into the influence of the degree of downtapering (the pitch in the taper waist) in the late taper design. This can be seen in Figs. 4(c) and 4(d). The *Late* taper design was chosen as it seems to give the best results in terms of 1) low noise, 2) average power in the red band and 3) the most flat spectrum in both the NIR and VIS ranges. For the VIS band, the noise improves almost linearly with the degree of tapering, i.e., with decreasing pitch in the taper waist. For the NIR band, the noise improvements pick up as the second ZDW approaches the band. The power decreases only slightly in the NIR band, while it increases significantly in the VIS band. The sudden decrease at 1.3 μm corresponds to when the second ZDW enters the NIR band. This can be explained by the clear depletion of spectral power around the second ZDW, that was earlier discussed. Interestingly the RIN, which includes the spectral power, is largely unaffected by this depletion of spectral power. SD-OCT systems usually only require a few mW of optical power to operate, so power at more than 0.5 W is not an issue. Nonetheless, taking both power and noise into account, there is an optimum in pitch at around 1.5 μm for the NIR band, while for the VIS band the optimum is slightly lower at 1.3 μm.

Let us now take a deeper look at why the noise is lowered in the tapers. In Fig. 5 we see spectrograms for a single shot simulation of the *Late* fiber design at different propagation distances, around the distance where the first solitons start to feel the second ZDW moving in from the loss edge due to tapering. In Fig. 5(a), before the effect of the second ZDW becomes

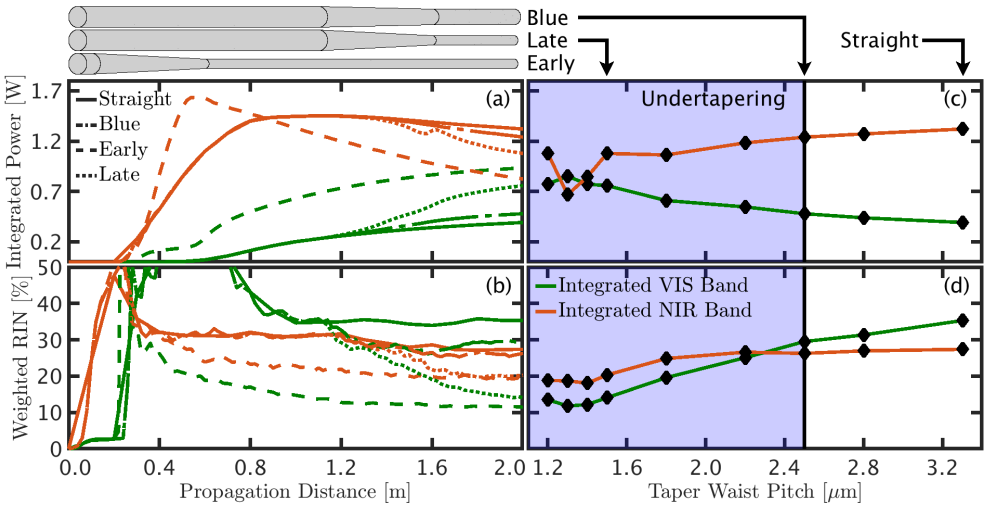

Fig. 4. Integrated power and weighted RIN for the two OCT bands shown in Fig. 3 (red=NIR, green=VIS). (a+b) Evolution versus propagation distance for all four cases shown in Fig. 2. (c+d) Output values versus degree of tapering (pitch in the waist) for the *Late* design. The fiber has an initial pitch of 3.3 μm and is then tapered to the pitch on the graph, with L_S = 1.1 m, L_T = 0.5 m and L_W = 0.4 m. Thus 1.5 μm and 2.5 μm correspond to the *Late* and *Blue* designs shown in the previous figures. The colored area marks the region of undertapering.

Optics EXPRESS

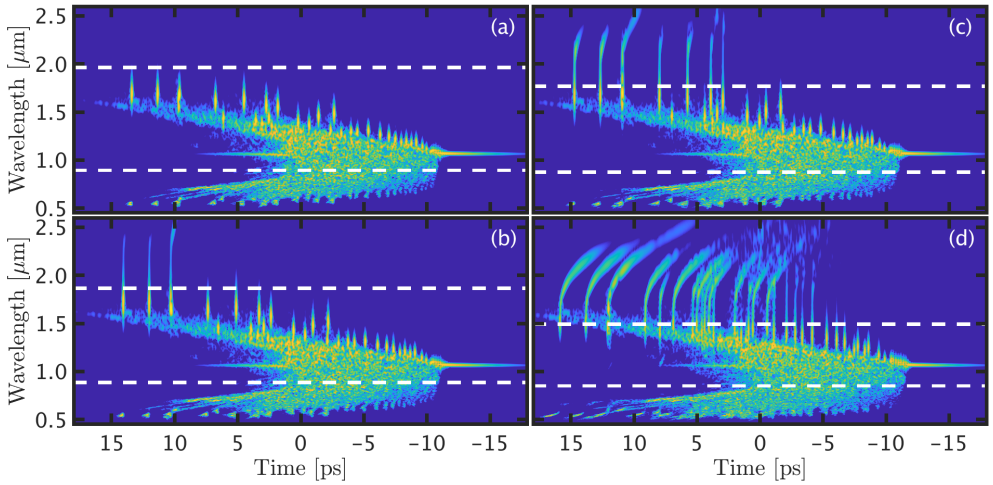

Fig. 5. Spectrograms for a single shot at different propagation distances in the *Late* fiber design: (a) $z = 1.50$ m, (b) $z = 1.52$ m, (c) $z = 1.54$ m and (d) $z = 1.6$ m. The spectrogram function used a 60 fs standard deviation, unnormalized gaussian envelope with an even 60 fs spacing in time. The white dashed lines denote zero dispersion wavelengths.

noticeable, we see the usual pattern expected from MI-induced SCG; several isolated and delayed large solitons near the loss edge excited by multiple collisions from the initial sea of solitons generated near the pump around the MI stokes wavelength. They have on average swallowed energy from many smaller solitons. The corresponding DW packets group-velocity matched to these large solitons are clearly seen at the blue edge [1].

In Figs. 5(b)-5(d), we see the effects of the second ZDW moving through the solitons spectrally. In established theory, when a soliton reaches the second ZDW through redshifting, it is spectrally recoiled while coupling a significant amount of energy to a phase-matched DW in the normal dispersion region across the ZDW, which typically halts the redshift about 50nm from the ZDW [33, 36, 52]. Here the second ZDW decreases so fast due to the tapering that it forces the solitons to come so close to the ZDW that they deliver almost all their energy to a band of DWs, which is spectrally broad because of the broad range of phase-matched wavelengths achieved during the down tapering. One can say that all solitons that before the taper were above or reasonably close to the second ZDW in the taper waist, $\lambda_{\mathrm{zdw2}}^{\mathrm{waist}}$=1500nm, become extruded through the ZDW into a band of DWs, which are not trapped by the solitons and therefore disperse temporally. Since the solitons are destroyed they also no longer can trap the DWs at the blue edge, which are clearly seen to disperse. Because a major part of the spectrum is now spectrally fixed by $\lambda_{\mathrm{zdw2}}^{\mathrm{waist}}$, all DWs above 1500 nm and all solitons halted by spectral recoil in an about 100nm broad band below $\lambda_{\mathrm{zdw2}}^{\mathrm{waist}}$, are spectrally overlapping and therefore we see a strong reduction in the ensemble averaged RIN above 1400 nm, which is also clearly visible in Fig. 3 (b).

In Fig. 6 we look closer at the spectral-temporal dynamics for the *Early* fiber design, for which the solitons have not reached $\lambda_{\mathrm{zdw2}}^{\mathrm{waist}}$ when the tapering starts. The dispersion curve in the waist slopes down above 1100 nm (see Fig. 1(a)), which speeds up the redshift of a soliton. This pulls out a significantly increased number of solitons from the sea of solitons around the MI stokes wavelength and rapidly redshifts them close to $\lambda_{\mathrm{zdw2}}^{\mathrm{waist}}$, where they stop redshifting due to spectral recoil while generating DWs in the normal dispersion region above $\lambda_{\mathrm{zdw2}}^{\mathrm{waist}}$. In fact the ZDWs are so close to the soliton sea in the waist that the random collisions appearing in the sea is reflected in the distribution of DWs because they directly generate new DWs at random wavelengths.

Optics EXPRESS

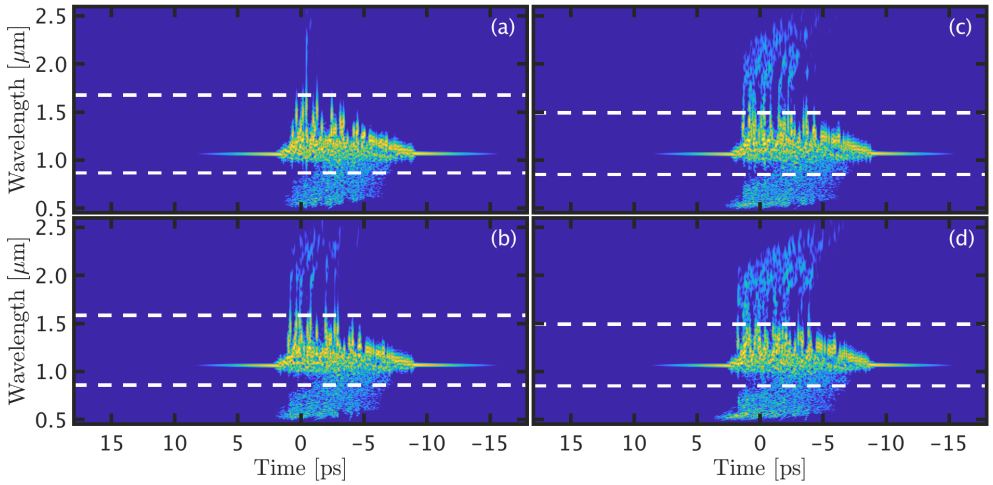

Fig. 6. The figure showns spectrograms for a single shot at different propagation distances in the *Early* fiber design: (a) $z = 0.56$ m, (b) $z = 0.58$ m, (c) $z = 0.60$ m and (d) $z = 0.62$ m. Spectrogram parameters are the same as those reported in Fig. 5.

Again we see a clear spectral overlap above 1400 nm due to the short $\lambda_{\mathrm{zdw2}}^{\mathrm{waist}}$, the same as for the *Late* design, which strongly reduces the noise through averaging, as seen in Fig. 3(b).

From Figs. 5 and 6 we can see that the position of the taper is extremely important for the physics, and even though the resulting output noise and spectral content might be almost the same, the fine structure is very different. Further improvements in noise might be observed if the initial straight fiber length, L_S, is increased to enable more solitons to pass the final second ZDW before they are extruded by the undertapering. However, the RIN at any wavelength is however never expected to be better than what is already observed at the pump.

Reductions in the length of the downtaper section, L_T, has been superficially investigated without any notable changes. Thus for the case of the *Early* fiber, the same good noise properties could be obtained by forgoing the taper completely and splicing the initial straight fiber to the straight fiber in the waist. In the *Late* fiber, it might not be the case as there would be no extrusion process to broaden the individual solitons. In either case, the losses due to mode mismatch would limit the applicability of this approach with respect to power.

The results presented here rely only on dispersion engineering and are independent of material, structure and wavelength. The results could thus be direcly applied to SCG in other fibers where low noise is of interest, such as chalcogenide fibers in the mid infrared region [53, 54]. With the advent of dispersion engineered specialty fibers [55], low noise SCG covering the whole molecular fingerprint region should be possible.

4. Conclusion

We have investigated numerically the effects of undertapering on the noise properties of a supercontinuum generated by modulation instability breaking up a long pump pulse. However, the results apply to any supercontinuum consisting of a large number of solitons and thus also to pumping with short femtosecond pulses with a high soliton number that undergo soliton fission.

The name undertapering refers to that the fiber is tapered to a diameter under the optimum diameter for achieving the shortest blue edge, such that the second ZDW decreases below the loss edge and starts to influence the nonlinear dynamics and thus the resulting supercontinuum spectrum.

Optics EXPRESS

We have demonstrated that undertapering strongly decreases the noise by spectrally aligning a large number of temporally separated parts of the supercontinuum to the short second ZDW in the taper waist, which leads to an inherent averaging. The predicted weighted RIN improvements of the VIS and NIR spectral bands of interest for optical coherence tomography was found to be from 35.3 % and 27.4 % to 14.0 % and 20.3 % respectively. The improvements are even more significant near the red spectral edge. Undertapering can be used to improve the noise performance of supercontinuum sources to make them more suitable for imaging applications, such as optical coherence tomography.

Funding

Innovation Fund Denmark (ShapeOCT-4107-00011A); GALAHAD Horizon 2020 Framework Programme (732613); Det Frie Forskningsraad (LOISE-4184-00532B).

References

1. J. M. Dudley, G. Genty, and S. Coen, "Supercontinuum generation in photonic crystal fiber," Rev. Mod. Phys. **78**, 1135–1184 (2006).
2. G. Agrawal, *Nonlinear Fiber Optics* (Elsevier, 2013), 5th ed.
3. J. Yi, W. Liu, S. Chen, V. Backman, N. Sheibani, C. M. Sorenson, A. A. Fawzi, R. A. Linsenmeier, and H. F. Zhang, "Visible light optical coherence tomography measures retinal oxygen metabolic response to systemic oxygenation," Light. Sci. & Appl. **4**, e334 (2015).
4. X. Shu, L. Beckmann, and H. F. Zhang, "Visible-light optical coherence tomography: a review," J. Biomed. Opt. **22,** 121707 (2017).
5. M. Maria, I. Bravo Gonzalo, T. Feuchter, M. Denninger, P. M. Moselund, L. Leick, O. Bang, and A. Podoleanu, "Q-switch-pumped supercontinuum for ultra-high resolution optical coherence tomography," Opt. Lett. **42**, 4744–4747 (2017).
6. D. J. Harper, M. Augustin, A. Lichtenegger, P. Eugui, C. Reyes, M. Glosmann, C. K. Hitzenberger, and B. Baumann, "White light polarization sensitive optical coherence tomography for sub-micron axial resolution and spectroscopic contrast in the murine retina," Biomed. Opt. Express **9**, 2115–2129 (2018).
7. N. M. Israelsen, M. Maria, M. Mogensen, S. Bojesen, M. Jensen, M. Hædersdal, A. Podoleanu, and O. Bang, "The value of ultrahigh resolution OCT in dermatology - delineating the dermo-epidermal junction, capillaries in the dermal papillae and vellus hairs," Biomed. Opt. Express **9**, 2240–2265 (2018).
8. M. Jensen, I. B. Gonzalo, R. D. Engelsholm, M. Maria, N. M. Israelsen, A. Podoleanu, and O. Bang, "Noise of supercontinuum sources in spectral domain optical coherence tomography," J. Opt. Soc. Am. B **36**, A154–A160 (2019).
9. D. R. Solli, C. Ropers, P. Koonath, and B. Jalali, "Optical rogue waves," Nature **450**, 1054–1057 (2007).
10. U. Møller, S. T. Sørensen, C. Jakobsen, J. Johansen, P. M. Moselund, C. L. Thomsen, and O. Bang, "Power dependence of supercontinuum noise in uniform and tapered PCFs," Opt. Express **20**, 2851–2857 (2012).
11. B. Wetzel, A. Stefani, L. Larger, P. A. Lacourt, J. M. Merolla, T. Sylvestre, A. Kudlinski, A. Mussot, G. Genty, F. Dias, and J. M. Dudley, "Real-time full bandwidth measurement of spectral noise in supercontinuum generation," Sci. Reports **2,** 882 (2012).
12. U. Moller and O. Bang, "Intensity noise in normal-pumped picosecond supercontinuum generation, where higher-order Raman lines cross into anomalous dispersion regime," Electron. Lett. **49**, 63–65 (2013).
13. T. Godin, B. Wetzel, T. Sylvestre, L. Larger, A. Kudlinski, A. Mussot, A. Ben Salem, M. Zghal, G. Genty, F. Dias, and J. M. Dudley, "Real time noise and wavelength correlations in octave-spanning supercontinuum generation," Opt. Express **21**, 18452 (2013).
14. M. Klimczak, B. S. Iwicki, B. Zhou, M. Bache, D. Pysz, O. Bang, and R. Buzcynski, "Coherent supercontinuum bandwidth limitations under femtosecond pumping at 2 m in all-solid soft glass photonic crystal fibers," Opt. Express **24**, 29406–29416 (2016).
15. A. M. Heidt, J. S. Feehan, J. H. V. Price, and T. Feurer, "Limits of coherent supercontinuum generation in normal dispersion fibers," J. Opt. Soc. Am. B **34**, 764–775 (2017).
16. I. B. Gonzalo, R. D. Engelsholm, M. P. Sorensen, and O. Bang, "Polarization noise places severe constraints on coherence of all- normal dispersion femtosecond supercontinuum generation," Sci. Reports **8**, 6579 (2018).
17. J. M. Dudley, G. Genty, F. Dias, B. Kibler, and N. Akhmediev, "Modulation instability, Akhmediev Breathers and continuous wave supercontinuum generation," Opt. Express **17**, 21497 (2009).
18. D. R. Solli, C. Ropers, and B. Jalali, "Active control of rogue waves for stimulated supercontinuum generation," Phys. Rev. Lett. **101**, 18–21 (2008).
19. A. V. Gorbach and D. V. Skryabin, "Light trapping in gravity-like potentials and expansion of supercontinuum spectra in photonic crystal fibres," Nat. Photonics **1**, 653–657 (2007).
20. P. Beaud, W. Hodel, B. Zysset, and H. Weber, "Ultrashort pulse propagation, pulse breakup, and fundamental soliton formation in a single-mode optical fiber," IEEE journal quantum electronics **23**, 1938–1946 (1987).

Optics EXPRESS

21. S. T. Sørensen, U. Møller, C. Larsen, P. M. Moselund, C. Jakobsen, J. Johansen, T. V. Andersen, C. L. Thomsen, and O. Bang, "Deep-blue supercontinnum sources with optimum taper profiles - verification of GAM," Opt. Express **20**, 10635–10645 (2012).
22. S. T. Sørensen, A. Judge, C. L. Thomsen, and O. Bang, "Optimum fiber tapers for increasing the power in the blue edge of a supercontinuum - group-acceleration matching," Opt. Lett. **36**, 816–818 (2011).
23. S. T. Sørensen, C. Larsen, C. Jakobsen, C. L. Thomsen, and O. Bang, "Single-mode pumped high air-fill fraction photonic crystal fiber taper for high-power deep-blue supercontinuum sources," Opt. Lett. **39**, 1097–1100 (2014).
24. A. Kudlinski, A. K. George, J. C. Knight, J. Travers, A. Rulkov, S. V. Popov, and J. Taylor, "Zero-dispersion wavelength decreasing photonic crystal fibers for ultraviolet-extended supercontinuum generation," Opt. Express **14**, 5715–5722 (2006).
25. A. Kudlinski, B. Barviau, A. Leray, C. Spriet, and A. Mussot, "Control of pulse-to-pulse fluctuations in visible supercontinuum," Opt. Express **18**, 27445–27454 (2010).
26. S. Pricking and H. Giessen, "Tailoring the soliton and supercontinuum dynamics by engineering the profile of tapered fibers," Opt. Express **18**, 20151–20163 (2010).
27. S. T. Sørensen, C. Larsen, U. Møller, P. M. Moselund, C. L. Thomsen, and O. Bang, "Influence of pump power and modulation instability gain spectrum on seeded supercontinuum and rogue wave generation," J. Opt. Soc. Am. B **29**, 2875–2885 (2012).
28. G. Genty, J. M. Dudley, and B. J. Eggleton, "Modulation control and spectral shaping of optical fiber supercontinuum generation in the picosecond regime," Appl. Phys. B **94**, 187–194 (2008).
29. G. Genty and J. M. Dudley, "Route to coherent supercontinuum generation in the long pulse regime," IEEE J. Quantum Electron. **45**, 1331–1335 (2009).
30. T. A. Birks, W. J. Wadsworth, and P. S. J. Russell, "Supercontinuum generation in tapered fibers," Opt. Lett. **25**, 1415 (2000).
31. J. C. Travers and J. R. Taylor, "Soliton trapping of dispersive waves in tapered optical fibers," Opt. Lett. **34**, 115–117 (2009).
32. K. M. Hilligsoe, T. V. Andersen, H. N. Paulsen, C. K. Nielsen, K. Mølmer, S. Keiding, R. Kristiansen, K. P. Hansen, and J. J. Larsen, "Supercontinuum generation in a photonic crystal fiber with two zero dispersion wavelengths," Opt. Express **12**, 1045 (2004).
33. P. Falk, M. H. Frosz, and O. Bang, "Supercontinuum generation in a photonic crystal fiber with two zero-dispersion wavelengths tapered to normal dispersion at all wavelengths," Opt. Express **13**, 7535–7540 (2005).
34. A. Efimov, A. J. Taylor, F. G. Omenetto, A. V. Yulin, N. Y. Joly, F. Biancalana, D. V. Skryabin, J. C. Knight, and P. S. Russell, "Time-spectrally-resolved ultrafast nonlinear dynamics in small-core photonic crystal fibers: Experiment and modelling," Opt. Express **12**, 6498 (2004).
35. P. Falk, M. H. Frosz, O. Bang, L. Thrane, P. E. Andersen, A. O. Bjarklev, K. P. Hansen, and J. Broeng, "Broadband light generation at approximately 1300 nm through spectrally recoiled solitons and dispersive waves," Opt. letters **33**, 621–623 (2008).
36. D. V. Skryabin, F. Luan, J. C. Knight, and P. S. J. Russell, "Soliton self-frequency shift cancellation in photonic crystal fibers," Science **301**, 1705–1708 (2003).
37. M. Koshiba and K. Saitoh, "Applicability of classical optical fiber theories to holey fibers," Opt. letters **29**, 1739–1741 (2004).
38. M. Kolesik, E. M. Wright, and J. V. Moloney, "Simulation of femtosecond pulse propagation in sub-micron diamter tapered fibers," Appl. Phys. B **79**, 293–300 (2004).
39. J. Laegsgaard, "Mode profile dispersion in the generalised nonlinear Schrödinger equation," Opt. Express **15**, 16110–16123 (2007).
40. F. Poletti and P. Horak, "Description of ultrashort pulse propagation in multimode optical fibers," J. Opt. Soc. Am. B **25**, 1645–1654 (2008).
41. O. Vanvincq, J. C. Travers, and A. Kudlinski, "Conservation of the photon number in the generalized nonlinear Schrödinger equation in axially varying optical fibers," Phys. Rev. A **84,** 063820 (2011).
42. J. Laegsgaard, "Modeling of nonlinear propagation in fiber tapers," J. Opt. Soc. Am. B **29**, 3183–3191 (2012).
43. P. M. Moselund, "Long-pulse supercontinuum light sources," Ph.D. thesis, Technical University of Denmark (2009).
44. I. B. Gonzalo and O. Bang, "Role of the Raman gain in the noise dynamics of all-normal dispersion silica fiber supercontinuum generation," JOSA B **35**, 2102–2110 (2018).
45. E. Gernier, P. Bowen, T. Sylvestre, J. Dudley, P. M. Moselund, and O. Bang, "Amplitude noise and coherence degradation of femtosecond supercontinuum generation in all-normal-dispersion fibers," J. Opt. Soc. Am. B **36**, A161–A167 (2019).
46. S. Rao D. S., R. D. Engelsholm, I. B. Gonzalo, B. Zhou, P. Bowen, P. M. Moselund, O. Bang, and M. Bache, "Ultra-low noise supercontinuum generation with flat near-zero normal dispersion fiber," arXiv preprint arXiv:1812.03877 (2018).
47. J. M. Dudley and S. Coen, "Coherence properties of supercontinuum spectra generated in photonic crystal and tapered optical fibers," Opt. Lett. **27**, 1180–1182 (2002).
48. K. L. Corwin, N. R. Newbury, J. M. Dudley, S. Coen, S. A. Diddams, K. Weber, and R. S. Windeler, "Fundamental Noise Limitations to Supercontinuum Generation in Microstructure Fiber," Phys. Rev. Lett. **90**, 113904 (2003).
49. K. L. Corwin, N. R. Newbury, J. M. Dudley, S. Coen, S. A. Diddams, B. R. Washburn, K. Weber, and R. S. Windeler,

Optics EXPRESS

"Fundamental noise limitations to supercontinuum generation in a microstructured fiber," Appl. Phys. B **77**, 269–277 (2003).
50. U. Møller, S. T. Sørensen, C. Larsen, P. M. Moselund, C. Jakobsen, J. Johansen, C. L. Thomsen, and O. Bang, "Optimum PCF tapers for blue-enhanced supercontinuum sources," Opt. Fiber Technol. **18**, 304–314 (2012).
51. J. Johansen, O. Bang, C. Larsen, T. Feuchter, T. V. Andersen, and C. L. Thomsen, "Microstructured optical fiber, supercontinuum light source comprising microstructured optical fiber and use of such light source," (2013). US Patent 9841557B2.
52. M. H. Frosz, P. Falk, and O. Bang, "The role of the second zero-dispersion wavelength in generation of supercontinua and bright-bright soliton-pairs across the zero-dispersion wavelength," Opt. Express **13**, 6181–6192 (2005).
53. I. Kubat, C. S. Agger, U. Møller, A. B. Seddon, Z. Tang, S. Sujecki, T. M. Benson, D. Furniss, S. Lamrini, K. Scholle, P. Fuhrberg, B. Napier, M. Farries, J. Ward, P. M. Moselund, and O. Bang, "Mid infrared supercontinuum generation to 12.5 μm in large NA chalcogenide step-index fibres pumped at 4.5 μm," Opt. express **22**, 19169–19182 (2014).
54. C. R. Petersen, R. D. Engelsholm, C. Markos, L. Brilland, C. Caillaud, J. Troles, and O. Bang, "Increased mid-infrared supercontinuum bandwidth and average power by tapering large-mode-area chalcogenide photonic crystal fibers," Opt. Express **25**, 15336–15347 (2017).
55. C. Markos, J. C. Travers, A. Abdolvand, B. J. Eggleton, and O. Bang, "Hybrid photonic-crystal fiber," Rev. Mod. Phys. **89**, 045003 (2017).